Contrib Mineral Petrol (2007) 154:663–674
DOI 10.1007/s00410-007-0215-7

ORIGINAL PAPER

# $H_2O$ storage capacity of $MgSiO_3$ clinoenstatite at 8–13 GPa, 1,100–1,400°C

**A. C. Withers · M. M. Hirschmann**

Received: 22 December 2006 / Accepted: 3 May 2007 / Published online: 1 June 2007


**Abstract** We present $H_2O$ analyses of $MgSiO_3$ pyroxene crystals quenched from hydrous conditions in the presence of olivine or wadsleyite at 8–13.4 GPa and 1,100–1,400°C. Raman spectroscopy shows that all pyroxenes have low clinoenstatite structure, which we infer to indicate that the crystals were high clinoenstatite (*C2/c*) during conditions of synthesis. $H_2O$ analyses were performed by secondary ion mass spectrometry and confirmed by unpolarized Fourier transform infrared spectroscopy on randomly oriented crystals. Measured $H_2O$ concentrations increase with pressure and range from 0.08 wt.% $H_2O$ at 8 GPa and 1,300°C up to 0.67 wt.% at 13.4 GPa and 1,300°C. At fixed pressure, $H_2O$ storage capacity diminishes with increasing temperature and the magnitude of this effect increases with pressure. This trend, which we attribute to diminishing activity of $H_2O$ in coexisting fluids as the proportion of dissolved silicate increases, is opposite to that observed previously at low pressure. We observe clinoenstatite 1.4 GPa below the pressure stability of clinoenstatite under nominally dry conditions. This stabilization of clinoenstatite relative to orthoenstatite under hydrous conditions is likely owing to preferential substitution of $H_2O$ into the high clinoenstatite polymorph. At 8–11 GPa and 1,200–1,400°C, observed $H_2O$ partitioning between olivine and clinoenstatite gives values of $D^{ol/CEn}$ between 0.65 and 0.87. At 13 GPa and 1,300°C, partitioning between wadsleyite and clinoenstatite, $D^{wd/CEn}$, gives a value of 2.8 ± 0.4.

Communicated by T.L. Grove.

A. C. Withers (✉) · M. M. Hirschmann
Department of Geology and Geophysics,
University of Minnesota, 108 Pillsbury Hall,
Minneapolis, MN 55455, USA
e-mail: anthony.c.withers-1@umn.edu

## Introduction

The $H_2O$ storage capacity of high pressure silicates is a topic of considerable importance for predicting and modelling the properties of the mantle and for understanding Earth's deep water cycle (e.g., Hirth and Kohlstedt 1996; Williams and Hemley 2001; Hirschmann et al. 2005; Hirschmann 2006; Komabayashi and Omori 2006; Smyth and Jacobsen 2006). There are now considerable data for the water storage capacity of olivine, the chief constituent of the upper mantle (Kohlstedt et al. 1996; Mosenfelder et al. 2006; Smyth et al. 2006), though uncertainties remain and more data are desirable. Less well known is the water storage capacity of the second most abundant mineral, pyroxene.

At shallow mantle conditions below ~3 GPa, the water content of pyroxene exceeds that of coexisting olivine by approximately a factor of 10 (Bell and Rossman 1992; Aubaud et al. 2004; Hirschmann et al. 2005; Hauri et al. 2006). For regions in the mantle where such strong partitioning prevails, pyroxene, rather than olivine, is the principal host of water. On the other hand, the storage capacity of olivine increases by up to three orders of magnitude with pressure (Kohlstedt et al. 1996; Mosenfelder et al. 2006; Smyth et al. 2006), and it is not clear whether pyroxene remains the primary host of $H_2O$ in deeper parts of the upper mantle.

Pyroxene $H_2O$ storage capacity is related to its complex chemistry. In pure $MgSiO_3$ pyroxene, H may be incorporated and charge balanced through the formation of cation

vacancies (e.g., Rauch and Keppler 2002). At least in some cases, $H^+$ is stabilised in the pyroxene structure as part of a coupled substitution with $Al^{3+}$ (Rauch and Keppler 2002; Aubaud et al. 2004; Hauri et al. 2006). The influences of other pyroxene substituents, including Ca, $Fe^{2+}$, $Fe^{3+}$, $Ti^{4+}$ and $Na^+$, are thought to be less important than that of $Al^{3+}$ (Rauch and Keppler 2002; Bromiley and Keppler 2004; Bromiley et al. 2004; Stalder 2004; Stalder et al. 2005), though available data are sparse, particularly for compositions of orthopyroxenes and clinopyroxenes similar to those typical of natural peridotite. Additionally, pyroxene compositions typical of mantle peridotite may exist in several different crystal structures, including orthopyroxene (OEn, *Pbca*), low clinopyroxene (LCEn, $P2_1/c$) and high clinopyroxene (HCEn, *C2/c*) and the storage capacity of a pyroxene may depend in part on its structural state. For example, Bromiley and Bromiley (2006) suggested that there are systematic differences in substitution mechanism for hydrogen among the $MgSiO_3$ polymorphs and that storage capacity may vary with structure. Bromiley and Bromiley (2006), Jacobsen et al. (2004), and Littlefield et al. (2005) found phase boundaries between the HCEn and LCEn phases of $MgSiO_3$ that are distinct from the stability fields determined from dry experiments (Angel and Hugh-Jones 1994) (Fig. 1), as would be expected if the polymorphs have different $H_2O$ storage capacities.

Most available constraints for the storage capacity of pyroxene are for the pyroxene with the simplest chemical composition, $MgSiO_3$ (Inoue et al. 1995; Rauch and Keppler 2002; Stalder and Skogby 2002; Mierdel and Keppler 2004; Yamada et al. 2004; Bromiley and Bromiley 2006). Rauch and Keppler (2002) used Fourier transform infrared spectroscopy (FTIR) to show that the storage capacity of $MgSiO_3$ pyroxene increases with pressure at 1,100°C, reaching a maximum of 0.087 ± 0.004 wt. % $H_2O$ at ~8 GPa and diminishing to 0.071 ± 0.004 wt. % $H_2O$ at 10 GPa. In contrast, Inoue et al. (1995) and Yamada et al. (2004) found between 0.32 and 0.8 wt. % $H_2O$ in $MgSiO_3$ clinoenstatite between 13 and 15 GPa and 1,300–1,500°C. These contrasting results have dramatically different ramifications for storage of $H_2O$ in the deep portions of the upper mantle. If the results of Rauch and Keppler (2002) are most applicable to natural mantle pyroxenes, then pyroxene hosts a negligible portion of the $H_2O$ in the deeper parts of the upper mantle and the storage capacity of the deep upper mantle is limited by the storage capacity of olivine. If the results of Inoue et al. (1995) and Yamada et al. (2004) are more relevant, then pyroxene may be a significant host of $H_2O$ throughout the upper mantle.

The apparent conflict between the modest storage capacities for $MgSiO_3$ orthoenstatite documented by Rauch and Keppler (2002) and the high storage capacities observed for $MgSiO_3$ clinoenstatite by Inoue et al. (1995) and Yamada et al. (2004) may be owing to differences in pyroxene structure (Fig. 1). Because the orthopyroxene structure is likely not stable in the convecting mantle at pressures greater than 8 GPa (Angel et al. 1992; Woodland 1998), it is the behaviour of clinopyroxene that is of greatest interest. Here we present new experimental data on the storage capacity of clinoenstatite at 8–13.4 GPa and 1,100–1,400°C.

## Methods

### Experiments

Reagent grade $SiO_2$, MgO and $Mg(OH)_2$ were mixed and ground under ethyl alcohol to yield a bulk composition of $3MgO–2SiO_2–2H_2O$. The starting material was loaded into 1.6 mm diameter AuPd capsules which were held in a water-cooled vice and sealed by welding. Experiments were performed in a 1,000-ton Walker-type multi-anvil device. For experiments at 7 and 8 GPa, anvils with 12 mm truncations, cast $MgO–Al_2O_3–SiO_2–Cr_2O_3$ octahedra with integrated gasket fins, and straight-walled graphite heaters (the ''12-TEL assembly'') were used. The pressure cali-

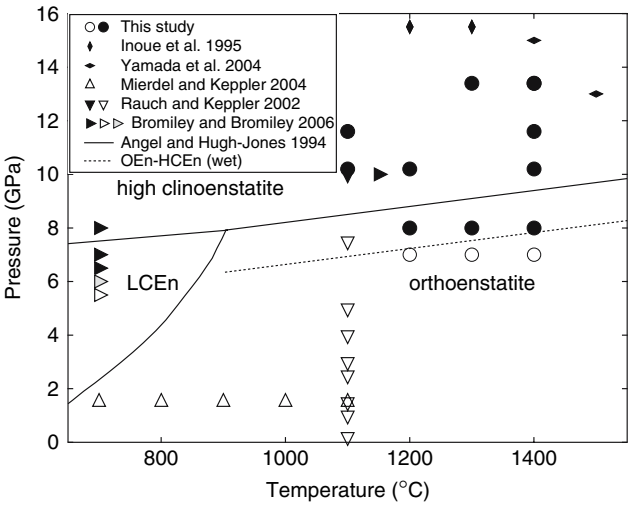


**Fig. 1** Temperatures and pressures of hydrous $MgSiO_3$ synthesis experiments from this study (*circles*) and from previous work compared to phase diagram for $MgSiO_3$, after Angel and Hugh-Jones (1994). *Vertical diamonds* from Inoue et al. (1995), *horizontal diamonds* from Yamada et al. (2004), *upward pointing triangles* from Mierdel and Keppler (2004), *downward pointing triangles* from Rauch and Keppler (2002) and *right pointing triangles* from Bromiley and Bromiley (2006). *Solid symbols* represent run products identified as low clinoenstatite transformed from high clinoenstatite, *open symbols* represent orthoenstatite and *shaded symbol* represents run product inferred to be equilibrium low clinoenstatite by Bromiley and Bromiley (2006). The *dashed line* indicates the approximate location of the OEn-CEn phase boundary in the presence of $H_2O$, based on the results of our synthesis experiments

bration for this assembly was established using multiple high temperature fixed points (Dasgupta et al. 2004). For experiments at 10.2–13.4 GPa, a 14–8 type assembly with pyrophyllite gaskets was used. Octahedra with 14 mm edge length, stepped $LaCrO_3$ heaters and $ZrO_2$ insulators were obtained from the COMPRES Multi-Anvil Cell Assembly Development Project. Details of the pressure calibration for this assembly are given in ''Appendix 1''. Run duration was 12 h for the experiment at 1,100°C and 6 h for all other experiments. Temperature was controlled with a $W_{97}Re_3/W_{75}Re_{25}$ thermocouple that was positioned immediately above the capsule and oriented axially with respect to the heater. *P–T* uncertainties are believed to be ±0.3 GPa, ±15°C for the 12-TEL assembly and ±0.5 GPa, ±30°C for the 14–8 assembly. Capsules were extracted from the pressure medium and sliced longitudinally using a wire saw, allowing textural and spatial relationships of the run products to be observed. One half of each capsule was impregnated with epoxy resin and reserved for electron microprobe analysis and optical and SEM observation, and crystals from the other half were prepared for secondary ion mass spectroscopy (SIMS) and Fourier transform infrared (FTIR) analyses.

## Secondary ion mass spectroscopy

Individual crystals were removed from the capsules, mounted in CrystalBond® and polished with diamond lapping films. After polishing, the crystals were removed from their polishing mounts by soaking in acetone, and were cleaned and mounted for SIMS analysis using the procedure described in Aubaud et al. (2007). Between 2 and 15 crystals from each experiment were mounted in indium, together with two hydrous volcanic glass standards (KN54Sta51 and JDF10, described in Aubaud et al. 2007) and a synthetic forsterite crystal with no detectable $H_2O$, which serves as a hydrogen blank. Run products were analyzed for H using the Cameca 6f at the GeoSIMS laboratory at Arizona State University.

A 5–10 nA primary $Cs^+$ beam was used to sputter the samples. The beam was rastered over a ~40 × 40 μm area prior to analysis to clean the analyzed area of surface-adsorbed contamination. The $Cs^+$ beam was tuned in aperture-illumination mode (Köhler illumination) to generate a uniform beam ~35 μm in diameter. The electron gun was tuned by adjusting the electromagnets from electron steering (to achieve co-linearity in y) and carefully placing an auxiliary permanent magnet between the transfer optics and electrostatic analyzer (for co-linearity in *x*). Negative secondary ions were accelerated from the sample (held at –9 kV). By utilizing the smallest field aperture (100 μm), only ions originating from the central ~10 μm area of a crater were counted. Ions with excess kinetic energies of 0 ±125 eV (energy bandpass centered and wide open) were allowed into the mass spectrometer, detected with an electron multiplier, and corrected for background and for counting system deadtime. Each measurement ran 6 cycles through the mass sequence, $^1H$, $^{12}C$, $^{19}F$ and $^{30}Si$, with counting times of 5, 10, 5, and 2 s, respectively. The intensities of the $^{12}C$ and $^{19}F$ signals have not been quantified, but were monitored to allow identification of contaminants, such as foreign material in cracks, that may give inaccurate measurements of hydrogen.

The calibration curves for H in pyroxene and olivine were established in the same session using the suites of pyroxenes and olivines described in Aubaud et al. (2007). The rigorous sample preparation and analytical protocols of Aubaud et al. (2007) resulted in background $^1H$ count rates of 45–70 cps when analysing the nominally dry forsterite blank.

To determine $H_2O$ concentrations, the mineral-specific calibrations of Aubaud et al. (2007) were used. The $H_2O$ contents of the pyroxene standards used by Aubaud et al. (2007) were determined using polarised FTIR and the Bell et al. (1995) calibration. Since the scatter in the data used to determine the cpx calibration curve is much greater than the opx curve, we used the latter to determine the $H_2O$ contents of LCEn. In the absence of a phase-specific calibration for wadsleyite, we used the olivine calibration for both forsterite and wadsleyite.

## Electron microprobe analysis

Major element concentrations were determined by wavelength-dispersive electron microprobe analysis with the JEOL JXA8900R at the University of Minnesota, using an acceleration voltage of 15 kV and 20 nA beam current, and ZAF data reduction with software supplied by JEOL. A focused beam (5 μm diameter) was used. The counting time was at least 10 s for each element and 5 s for the background. Mineral standards from Jarosewich et al. (1980) were used.

## Fourier transform infrared spectroscopy

Polished sections were prepared from a few of the larger crystals and analysed using a Nicolet Series II Magna-IR 750 spectrometer equipped with a Nic-Plan microscope, globar source, KBr beamsplitter and liquid nitrogen cooled MCT-A detector. Unpolarised infrared radiation was used. Even though absorption of unpolarised infrared radiation by unoriented, anisotropic samples cannot be scaled by path length in a truly quantitative manner (e.g., Libowitzky and Rossman 1996), infrared spectra were nevertheless normalized to sample thickness to provide a semi-quantitative comparison between absorption intensities. Sample

thicknesses were measured using a high-precision mechanical microscope stage, and are accurate to ±2 μm.

### Raman spectroscopy

Raman spectra were collected with a Witec Alpha300R confocal Raman microscope using the excitation from a 514.5 nm laser and a 1,800 $mm^{-1}$ grating. Spectra were averaged from ten accumulations, each with counting times of 10 s. Phase identification was made on the basis of characteristic peaks for orthoenstatite and clinoenstatitite described by Ulmer and Stalder (2001). Accordingly, clinoenstatite was distinguished from orthoenstatite by the presence of peaks at 369 and 431 $cm^{-1}$ and the shift of the peak near 243 $cm^{-1}$ down to 236 $cm^{-1}$.

## Results

Vertical sections through the retrieved experimental capsules revealed 20–500 μm crystals arranged in an ''hourglass'' pattern, and quench material, consisting of a mesh of crystalline precipitate and void space previously occupied by exsolved fluid, occupying the hottest part of the capsule (Fig. 2). Because the quench material consists mainly of void space and is poorly preserved during sample preparation, compositional analysis with the electron microprobe was not possible. Textural observations cannot be unequivocally interpreted, so we cannot speculate as to the nature of the equilibrium fluid/melt in the experiments. While we noted a general increase in the proportion of quench material with increasing temperature, suggesting an increase in dissolved silicate component, we could not acquire quantitative estimates of the composition of the quenched fluid or melt. Crystals were optically clear and colourless, and were euhedral to subhedral in habit. Electron microprobe analysis confirmed the presence of $MgSiO_3$ and $Mg_2SiO_4$ phases in all experiments other than the experiment at 13.4 GPa and 1,400°C, in which clinoenstatite was the only identified crystalline phase. Analyses further indicate that olivine and pyroxene are stoichiometric and lack measurable quantities of $Al_2O_3$ or other non-Mg/Si/H substituents (Table 1).

Raman spectra of $MgSiO_3$ phases were used to distinguish enstatite polymorphs based on the criteria of Ulmer and Stalder (2001) and indicate that all charges recovered from pressures ≥8 GPa contained low clinoenstatite, and that orthoenstatite was present in the 7 GPa experiments (Fig. 3). Forsterite was the stable $Mg_2SiO_4$ polymorph in experiments at 7–11.6 GPa, and wadsleyite was present in the experiment at 13.4 GPa and 1,300°C. Stabilization of wadsleyite relative to olivine at 13.4 GPa under hydrous conditions is consistent with the data of Chen et al. (2002) and Smyth and Frost (2002), allowing for ~1 GPa uncertainty in interlaboratory pressure calibrations.

Infrared spectra of LCEn show at least 9 absorption bands in the OH stretching region between 3,000 and 3,750 $cm^{-1}$ (Fig. 4). The calibrations of Bell et al. (1995) and Paterson (1982) were used to calculate $H_2O$ concentrations, notwithstanding the inaccuracies associated with unpolarised measurements of anisotropic samples (Table 2). Hydrogen contents of LCEn, olivine and wadsleyite determined using SIMS are given in Table 1, and the $H_2O$ concentrations in LCEn are plotted against synthesis pressure and temperature in Figs. 5 and 6.

Quantitative analysis of $H_2O$ in silicate from unpolarised infrared analyses of unoriented single crystals has a number sources of uncertainty, including those arising from the choice of baseline and calibration coefficient. Based on the polarised FTIR measurements of Bromiley and Bromiley (2006), we calculate that the integrated area of the OH stretching bands in randomly oriented clinoenstatite varies by up to 10% from the average axial polarised measurements, for our measured sample thicknesses. A greater source of uncertainty arises from the choice of baseline. The difficulty in choosing a baseline is compounded by the broad-band absorbance that appears to underlie the sharp peaks in orthoenstatite and clinoenstatite spectra, as discussed by Mierdel and Keppler (2004). The broad-band absorption is roughly equal in intensity to that of the sharp peaks, and most likely should be included in the estimation of $H_2O$ concentrations, but defining a baseline that includes the broad-band absorption is troublesome. Baseline subtractions from the spectra in Fig. 4 leave some broad-band component that has been included in the integration to estimate $H_2O$ concentrations. Concentration of $H_2O$ may be calculated using either a sample-independent general calibration that takes into consideration the dependence of extinction coefficient on frequency (Paterson 1982; Libowitzky and Rossman 1997), or the clinopyroxene-specific calibration of Bell et al. (1995). Both are reported in Table 2. However, the mineral-specific calibration may be preferred over the more general type, provided that the band positions, shapes and relative intensities are similar in the standard used for calibration and the unknown. In comparison to the calibration of Paterson (1982), the Bell et al. (1995) calibration for clinopyroxene results in $H_2O$ concentrations that are about 40% higher. The cumulate effect of these uncertainties leads us to believe that the accuracy of our IR measurements is in the order of 50%, while precision is estimated to be 10%.

SIMS measurements of $H_2O$ in clinoenstatite range from 0.08 ± 0.04 to 0.67 ± 0.08 wt.% (Table 2). Those measured by FTIR (using the calibration of Bell et al. 1995) range from 0.12 to 0.49 wt. %. Measurements made using

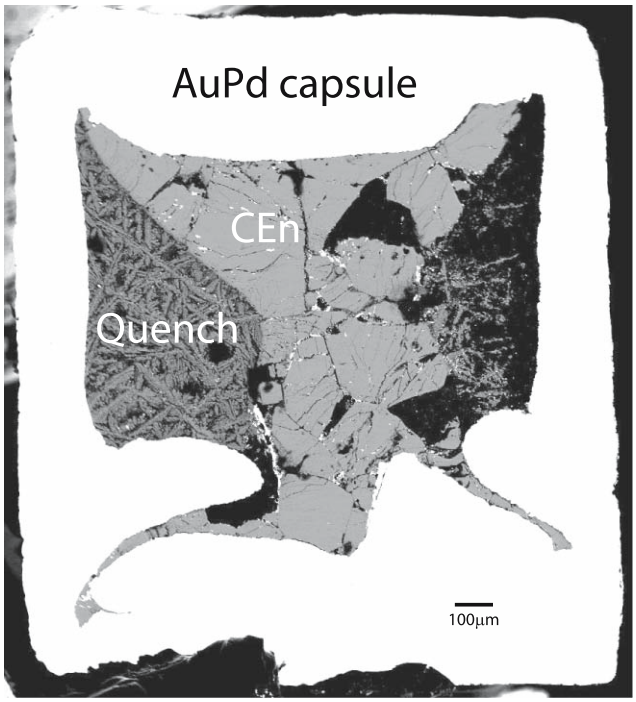


**Fig. 2** Backscattered electron image micrographs of a longitudinal section through the gold-palladium capsule of an experiment at 13.4 GPa, 1,400°C. Inside the capsule, a crudely hourglass-shaped region consists of clinoenstatite, which is surrounded by crystals quenched from a silicate-rich hydrous fluid. The black areas in between the crystals are epoxy resin infilling the space left by crystals plucked from the capsule by the wire saw or during polishing. Rounded black areas within the quenched material are artefacts introduced during sample preparation

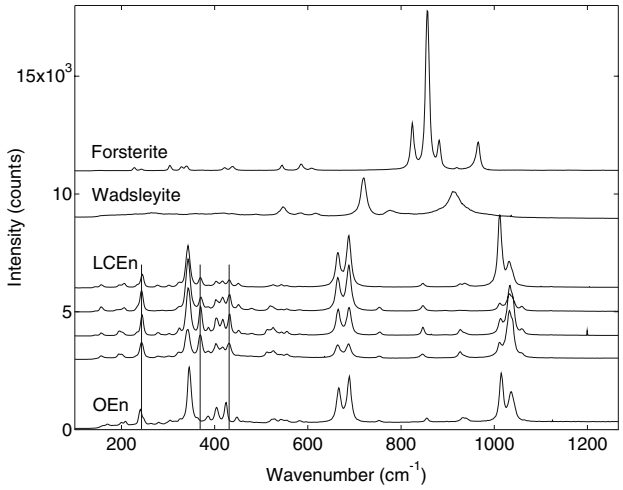


**Fig. 3** Raman spectra of randomly oriented crystals used for phase identification. *Vertical lines* indicate the positions of diagnostic peaks for low clinoenstatite (Ulmer and Stalder 2001). Spectra have been offset vertically, without further background treatment

FTIR and SIMS are generally consistent with one another within the estimated uncertainties of the measurements (Fig. 7). Concentrations in olivine at 8–11 GPa range from 0.08 ± 0.01 to 0.12 ± 0.02 wt.% and the wadsleyite quenched from 13 GPa and 1,300°C has 1.87 ± 0.10 wt. % $H_2O$. The storage capacities of olivine at 8–11.6 GPa (0.08–0.19%) are a little lower than observed by Mosenfelder et al. (2006) and Smyth et al. (2006) at similar pressures and temperatures. These differences may be partly owing to discrepancies in analytical calibrations. The measured storage capacity for wadsleyite is consistent with that observed by Demouchy et al. (2005).

## Discussion

### FTIR spectra

All IR spectra for clinoenstatite are similar to those reported by Rauch and Keppler (2002) and by Bromiley and Bromiley (2006) for low-clinoenstatite transformed from high-clinoenstatite. The broad peak at 3,040 $cm^{-1}$ and the major peak at 3,377 $cm^{-1}$ observed in the previous studies are present in all spectra, but are diminished relative to the sharp absorption bands at higher frequencies. The high frequency bands at 3,601, 3,676 and 3,688 $cm^{-1}$ are present in all previously published clinoenstatite spectra (Rauch and Keppler 2002; Bromiley and Bromiley 2006), but they are more prominent in the forsterite- and wadsleyite-buffered crystals from this study than from quartz-, coesite- or stishovite-buffered crystals (Rauch and Keppler 2002; Bromiley and Bromiley 2006). These same peaks are also present in a spectrum of orthoenstatite that was synthesised in the presence of forsterite by Rauch and Keppler (2002) at 3 GPa and 1,100°C. It is therefore likely that these bands are associated with a substitution mechanism that involves

**Table 1** Electron microprobe analysis of selected olivine and clinoenstatite crystals

| Experiment[a] | $n$[b] | $SiO_2$ | $TiO_2$ | $Al_2O_3$ | $Cr_2O_3$ | FeO | MnO | MgO | CaO | $Na_2O$ | Total |
|---|---|---|---|---|---|---|---|---|---|---|---|
| M268 ol | 1 | 42.82 | 0.068 | 0.000 | 0.031 | 0.00 | 0.003 | 57.18 | 0.003 | 0.000 | 100.10 |
| M268 cen | 3 | 59.96(27) | 0.01(2) | 0.01(1) | 0.000(0) | 0.01(1) | 0.01(2) | 39.94(12) | 0.004(4) | 0.002(3) | 99.95 |
| M264 cen | 7 | 59.82(38) | 0.01(2) | 0.008(7) | 0.01(2) | 0.01(1) | 0.001(4) | 39.69(17) | 0.02(2) | 0.002(4) | 99.57 |
| M270 cen | 3 | 59.07(20) | 0.01(1) | 0.01(1) | 0.03(1) | 0.01(1) | 0.00(1) | 39.98(4) | 0.02(2) | 0.00(1) | 99.13 |

[a] Experiment label and phase: ol=olivine, cen=clinoenstatite

[b] Number of crystals analysed

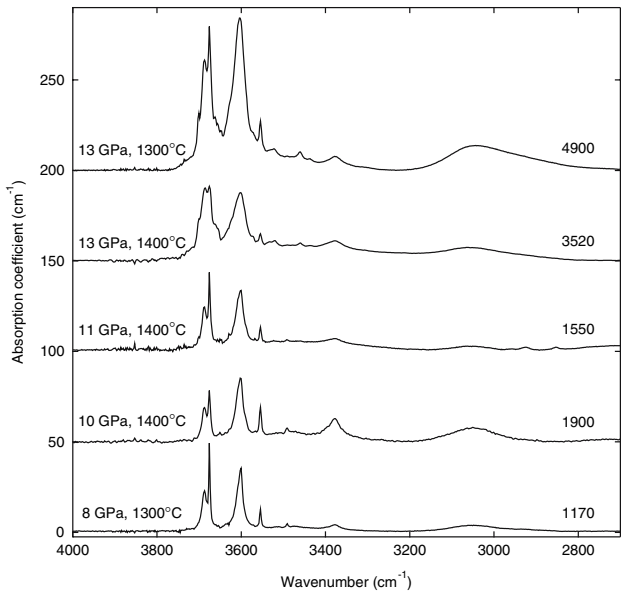


**Fig. 4** Unpolarised FTIR spectra of selected clinoenstatites from this study. Spectra are annotated with synthesis conditions and $H_2O$ concentration (in ppm) determined using the calibration of Bell et al. (1995). Baselines have been fit by eye to the region between 2,200 and 3,800 $cm^{-1}$

Si vacancies, and that this mechanism is enhanced in clinoenstatite over orthoenstatite, and becomes dominant in clinoenstatite under conditions of low silica activity.

The highest frequency bands at 3,676 and 3,688 $cm^{-1}$ are similar to bands attributed to amphibole lamellae in diopside (Ingrin et al. 1989; Skogby et al. 1990). However, these same bands are also observed by Bromiley and Bromiley (2006) for low clinoenstatite as well as for the crystal synthesized in the HCEn stability field at 10 GPa by Rauch and Keppler (2002). Given that our experiments are far from the limits of stability of amphibole in the system $MgO–SiO_2–H_2O$ (Chernosky et al. 1985; Evans and Ghiorso 1995) and of amphibole lamellae in $MgSiO_3$ pyroxene documented by Rauch and Keppler (2002), we infer that these high frequency bands are either intrinsic to the low clinoenstatite structure or are from hydrous lamellae developed during quench and/or depressurization. If the latter is true, the OH responsible for these bands was originally contained within the high clinoenstatite structure prior to quench, and therefore should be incorporated into measurements of HCEn storage capacity.

## $H_2O$ storage capacity of $MgSiO_3$ pyroxene

Compared with the water concentrations determined using SIMS, the FTIR measurements give broadly similar results (Table 2; Fig. 7), albeit with slightly higher concentrations for the low pressure experiments and lower concentrations for the higher pressure experiments, resulting in a smaller range of values. We have greater confidence in the SIMS measurements because the FTIR data are unpolarized measurements from a small number of unoriented single crystals, and hence likely do not represent a statistically valid sampling of the vibrational indicatrices of the crystals from the experiments. Thus, for the purposes of comparison, the following discussion is based on the SIMS measurements, unless otherwise specified. Importantly, the general pressure and temperature trends that we infer from SIMS data with pressure and temperature are confirmed by the infrared measurements. Also, comparisons between our data and those of other studies yield similar conclusions, irrespective of whether the FTIR or SIMS data are applied.

Concentrations of $H_2O$ in quenched $MgSiO_3$ from our experiments increase broadly with pressure (Fig. 5). At 13.4 GPa, the $H_2O$ contents that we infer for HCEn (Table 2) are consistent with those previously determined by Inoue et al. (1995) and Yamada et al. (2004) between 13 and 15.5 GPa. Also, the $H_2O$ contents found for HCEn at 8 GPa and 1,300–1,400°C (800–900 ppm) are similar to that found for OEn at 7.5 GPa and 1,100°C (867 ± 35 ppm) by Rauch and Keppler (2002). On the other hand, the concentrations of $H_2O$ that we observe at 10.2 GPa and 1,000–1,100°C (2,900–3,200 ppm) are significantly greater than the 714 ± 35 ppm found by Rauch and Keppler (2002) for HCEn at 10 GPa and 1,100°C. The difference may arise because the enstatite in our study was buffered by olivine whereas that of Rauch and Keppler (2002) was buffered by stishovite. This different buffering condition can influence the storage capacity in two different ways. First, the enstatite crystals may have different point defect populations. Second, the fluid coexisting with the assemblage enstatite plus stishovite likely had larger amounts of dissolved silicate than that coexisting with enstatite plus forsterite (Stalder et al. 2001) and consequently could have lower $H_2O$ activity. Although experiments at 1.5 and 3 GPa show little dependence of the storage capacity on the buffering phase (Rauch and Keppler 2002; Mierdel and Keppler 2004), this may not remain true at higher pressure, where the dissolved silicate component has a greater influence on water activities.

Our results affirm the large high pressure storage capacities of HCEn $MgSiO_3$ reported by Inoue et al. (1995) and Yamada et al. (2004). But at the same time, they are consistent with the low pressure results of Rauch and Keppler (2002). Together, these data indicate that the storage capacity of $MgSiO_3$ remains modest with increasing pressure in the stability field of orthopyroxene , but increases significantly in the stability field of clinopyroxene.

**Table 2** Experiment results

| Experiment | Pressure (GPa) | Temperature (°C) | Phases[a] | LCEn[b] (wt.% $H_2O$) | $n$[c] | Bell[d] (wt.% $H_2O$) | Paterson[e] (wt.% $H_2O$) | Fo[b] (wt.% $H_2O$) | $n$[c] | Wd[b] (wt.% $H_2O$) | $n$[c] | $D^{ol/px}$ |
|---|---|---|---|---|---|---|---|---|---|---|---|---|
| M326 | 7.0 | 1200 | E, O, Q | | | | | | | | | |
| M324 | 7.0 | 1300 | E, O, Q | | | | | | | | | |
| M325 | 7.0 | 1400 | E, O, Q | | | | | | | | | |
| M266 | 8.0 | 1200 | C, O, Q | | | | | 0.11 (1) | 7 | | | |
| M269 | 8.0 | 1300 | C, O, Q | 0.079 (4) | 4 | 0.12 | 0.08 | | | | | |
| M268 | 8.0 | 1400 | C, O, Q | 0.09 (2) | 5 | | | 0.08 (1) | 5 | | | 0.87 (23) |
| M272 | 10.2 | 1100 | C, O, Q | 0.32 (7) | 2 | | | | | | | |
| M255 | 10.2 | 1200 | C, O, Q | 0.29 (3) | 2 | | | 0.19 | 1 | | | 0.65 |
| M262 | 10.2 | 1400 | C, O, Q | 0.13 (3) | 6 | 0.19 | 0.11 | 0.09 (1) | 6 | | | 0.69 (16) |
| M274 | 11.6 | 1100 | C, O, Q | 0.28 (8) | 4 | | | | | | | |
| M273 | 11.6 | 1400 | C, O, Q | 0.14 (1) | 4 | 0.16 | 0.11 | 0.12 (2) | 2 | | | 0.82 (12) |
| M270 | 13.4 | 1300 | C, W, Q | 0.67 (8) | 4 | 0.49 | 0.35 | | | 1.87 (10) | 4 | 2.8 (4) |
| M264 | 13.4 | 1400 | C, Q | 0.43 (8) | 10 | 0.35 | 0.23 | | | | | |

[a] Phases identified using Raman spectroscopy. E=orthoenstatite, C=low clinoenstatite after high clinoenstatite, O=forsterite, W=wadsleyite, Q=quenched hydrous fluid/melt

[b] $H_2O$ concentration determined by SIMS. Uncertainties in parentheses are ±1SD in the least significant digit, i.e., 0.09(2) should be read as a value of 0.09 with SD 0.02

[c] Number of SIMS analyses

[d] LCEn $H_2O$ content calculated from unpolarised FTIR spectra using calibration of Bell et al. (1995)

[e] LCEn $H_2O$ content calculated from unpolarised FTIR spectra using calibration of Paterson (1982), assuming an orientation factor of 1/3

### Influence of temperature

As illustrated in Fig. 6, $H_2O$ storage capacity for $MgSiO_3$ compiled from our experiments as well as from previous results diminishes with increasing temperature at 10.2–11.6 GPa and 13–15.5 GPa. Little change with temperature is observed at 8 GPa. The decrease in $H_2O$ storage capacity with increasing temperature is the opposite of increases with temperature observed at 1.5 GPa by Mierdel and Keppler (2004). These distinct effects of temperature at low and high pressure are not unexpected (Hirschmann et al. 2005). At low pressure, the fluid coexisting with magnesian silicates has only a small proportion of dissolved silicate (Stalder et al. 2001; Mibe et al. 2002) and therefore the activity of $H_2O$ changes little with increasing temperature. Changes in $H_2O$ storage capacity largely reflect changes in solubility of $H_2O$ in the crystal at near-constant $H_2O$ activity. At high pressure, there is a larger proportion of dissolved silicate in hydrous fluid coexisting with magnesian silicate and the concentration of dissolved silicates changes appreciably with increasing temperature (Stalder et al. 2001). Consequently, at high pressure, increasing temperature results in diminishing activity of $H_2O$ and a corresponding decrease in $H_2O$ storage capacity of the coexisting crystals.

The decrease in $H_2O$ storage capacity with increasing temperature is the opposite of that predicted by the model of $H_2O$ storage capacity for $MgSiO_3$ enstatite by Mierdel and Keppler (2004) (Fig. 6). Because the only data constraining the temperature dependence of their model are from 1.5 GPa and $\leq$ 1,100°C, where the dependence is positive, their model cannot capture the decrease in storage capacity with temperature that prevails at higher pressures. Consequently, extrapolation of the Mierdel and Keppler (2004) model to high temperature high pressure conditions representative of the deep convecting upper mantle (1,400–1,600°C at 8–14 GPa; Ita and Stixrude 1992) will not be reliable and application to intermediate pressures (2–8 GPa) may also be hazardous. An additional consideration is that the Mierdel and Keppler (2004) model is calibrated chiefly from crystals buffered by silica phases whereas pyroxenes in the mantle coexist with olivine.

### Partitioning of $H_2O$ between clinoenstatite and olivine polymorphs

In the shallow mantle, $H_2O$ partitions strongly into pyroxene relative to olivine, with typical values of $D_H^{Ol/En}$ near 0.1 (Bell and Rossman 1992; Aubaud et al. 2004; Hirschmann et al. 2005; Hauri et al. 2006). We find values of $D_H^{Ol/En}$ between 0.65 and 0.89, meaning $H_2O$ prefers $MgSiO_3$ clinopyroxene relative to olivine in the deeper portions of the upper mantle, but that the preference is not as strong as at shallower depths. Also, our measured stor-

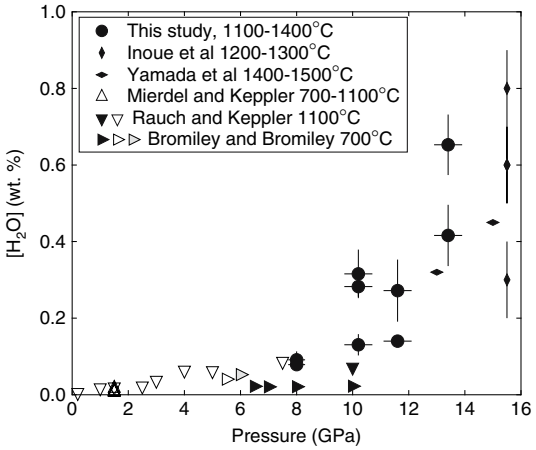


**Fig. 5** Concentration of $H_2O$ measured in $MgSiO_3$ as a function of synthesis pressure. *Circles* are SIMS measurements from this study, *vertical diamonds* from Inoue et al. (1995), *horizontal diamonds* from Yamada et al. (2004), *upward pointing triangles* from Mierdel and Keppler (2004), *downward pointing triangles* from Rauch and Keppler (2002) and *right pointing triangles* from Bromiley and Bromiley (2006). *Solid symbols* represent run products identified as low clinoenstatite transformed from high clinoenstatite, *open symbols* represent orthoenstatite and *shaded symbol* represents run product inferred by Bromiley and Bromiley (2006) to be equilibrium low clinoenstatite

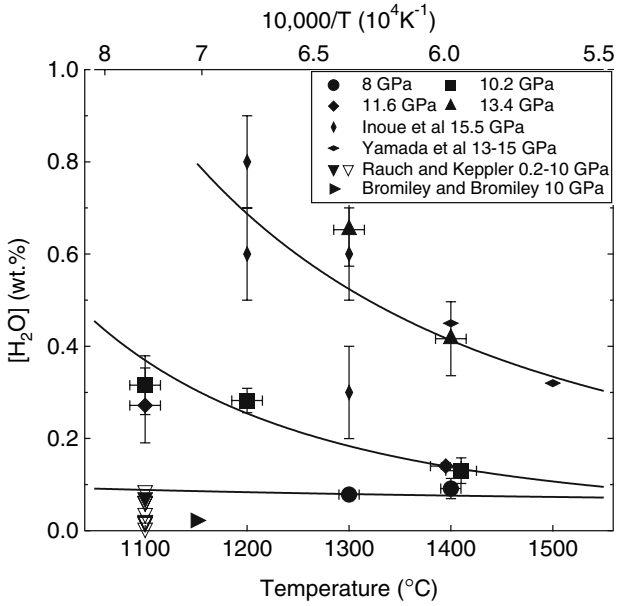


**Fig. 6** Concentrations of $H_2O$ measured in $MgSiO_3$ as a function of synthesis temperature. *Circles, diamonds, squares* and *upward pointing triangles* are SIMS measurements from this study. *Vertical diamonds* from Inoue et al. (1995), *horizontal diamonds* from Yamada et al. (2004), *downward pointing triangles* from Rauch and Keppler (2002) and *right pointing triangle* from Bromiley and Bromiley (2006). *Solid symbols* represent run products identified as low clinoenstatite transformed from high clinoenstatite and *open symbols* represent orthoenstatite. The *curves* are linear fits in reciprocal temperature space. The *uppermost curve* was fit to 13.4 GPa data from this study, together with 13–15.5 GPa data from Inoue et al. (1995) and Yamada et al. (2004). The *centre curve* was fit to 10.2 and 11.6 GPa data from this study and the *lowermost curve* to 8 GPa data from this study, using data from Rauch and Keppler (2002) and determinations of $D^{ol/cen}$ (Table 1) and measured storage capacity for olivine at 8 GPa and 1,200°C to constrain the curve at 1,100–1,200°C. Data at 10.2 and 11.6 GPa and 1,400°C have been offset for clarity

age capacities at 8–11.6 GPa and at 1,100–1,200°C are broadly similar to those measured for olivine at these temperatures, based on the measurements of Kohlstedt et al. (1996) increased by a factor of 3 (Bell et al. 2003) and the data of Mosenfelder et al. (2006). However, various substitutional complexities, such as $Al^{3+}$, should increase the storage capacity for $H_2O$ in pyroxene (Rauch and Keppler 2002), meaning that values of $D_H^{Ol/CEn}$ for natural mantle compositions are likely smaller than measured here. Similarly, small values of $D_H^{Ol/Pyx}$ at low pressure are related to the compositional complexity of natural orthopyroxene, and particularly to high Al contents (Bell and Rossman, 1992; Aubaud et al. 2004; Hirschmann et al. 2005; Hauri et al. 2006), so values of $D_H^{Ol/Pyx}$ appropriate for natural rocks in the deeper upper mantle are quite probably larger than those measured here. In an isochemical mantle, decreases in values of $D_H^{Ol/Pyx}$ with depth will lead to progressive increases in the proportion of $H_2O$ stored in olivine, which will have a tendency of reducing the creep strength of the upper mantle (Hirth and Kohlstedt 1996) with increasing depth, though the effects of increasing pressure likely counteract this tendency.

Owing to its high propensity to incorporate $H_2O$, wadsleyite likely dominates the $H_2O$ storage capacity of the upper portions of the transition zone. Pyroxene is a minor constituent of the upper transition zone, with a mode near 10% (Irifune and Isshiki 1998), and hence may make a secondary contribution to the storage capacity below 410 km. At 13.4 GPa, we observe a single value of $D_H^{Wd/CEn}$ of 2.8 ± 0.4 (Table 2). This is of similar magnitude but slightly smaller than values between 3.3 and 5.2 observed for $D_H^{Wd/CEn}$ in previous studies at 15–15.5 GPa (Inoue et al. 1995; Bolfan-Casanova et al. 2000) (Fig. 8).

## Influence of $H_2O$ on the HCEn/OEn phase boundary

$MgSiO_3$ pyroxene crystals synthesized at 8 GPa and 1,300–1,400°C in this study are inferred to have been HCEn at the conditions of synthesis, even though these conditions lie in the stability field of $MgSiO_3$ OEn established by nominally dry experiments (Angel and Hugh-Jones 1994; Shinmei et al. 1999; Ulmer and Stalder 2001). At 8 GPa and 1,400°C we observe HCEn 1.4 GPa lower than the phase boundary inferred from nominally dry experiments, which is too great an apparent discrep-

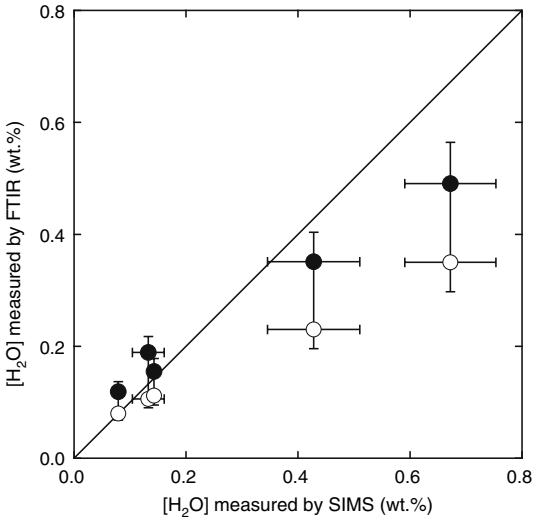


**Fig. 7** Comparison of $H_2O$ concentrations measured for $MgSiO_3$ clinoenstatite in this study by SIMS and by FTIR. The higher concentrations determined by FTIR (*solid symbols*) result from application of the Bell et al. (1995) calibration, and the corresponding lower values (*open symbols*) result from the Paterson (1982) calibration

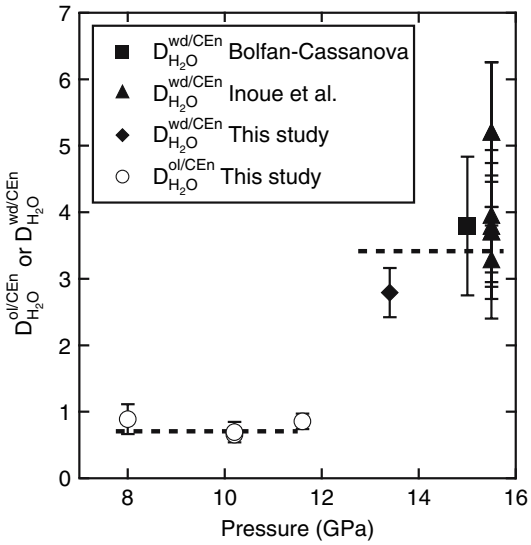


**Fig. 8** Olivine/enstatite and wadsleyite/enstatite partitioning of $H_2O$ from this study (*open circles* and *solid diamond*) and from previous studies (*square* from Bolfan-Casanova et al. 2000 and *triangles* from Inoue et al. 1995) as a function of pressure. Dashed lines are weighted averages of the partition coefficients

ancy to attribute to inter-laboratory differences in pressure calibrations. Rather, we infer that HCEn is stabilized relative to OEn under conditions of high water fugacity. We note, however, that our data do not define the limit of stability of HCEn, as they are from unreversed synthesis experiments.

We attribute the enhanced stability of HCEn under hydrous conditions to an increased $H_2O$ storage capacity of HCEn relative to OEn. This is consistent with in situ diamond anvil observations at room temperature, which show that $H_2O$ in $MgSiO_3$ expands the stability field of HCEn relative to LCEn (Jacobsen et al. 2004; Littlefield et al. 2005), suggesting that water partitions into HCEn in preference to the LCEn structure. Similarly, Bromiley and Bromiley (2006) inferred HCEn stability for crystals quenched from hydrous conditions at 700°C and 6.5, 1 GPa lower than the HCEn/LCEn stability boundary (Fig. 1). Greater storage capacity of HCEn relative to LCEn may be owing to further distortion of the M2 site required in the HCEn structure, which may be promoted by M-site vacancies required by OH substitution in the pure-Mg enstatite system. (S. Jacobsen, written communication 2006). In contrast, Rauch and Keppler (2002) inferred that the storage capacity of HCEn may be lower than that of OEn, based on comparison of OEn that they synthesized at 1,100°C and 8 GPa versus HCEn synthesized at 1,100°C and 10 GPa. However, our 10 GPa results at similar conditions (1,100–1,200°C) suggest considerably greater $H_2O$ storage capacity than observed by Rauch and Keppler (2002) (714 ± 35 ppm). We suggest that the higher silica activity imposed by the presence of excess silica in the experiments of Rauch and Keppler (2002) inhibits a substitution mechanism that accounts for much of the $H_2O$ content of the clinoenstatite from our experiments.

It has been speculated (Angel et al. 1992; Woodland 1998) that the HCEn/OEn phase boundary may be responsible for the so-called X discontinuity that is observed in some localities at depths near 300 km (Revenaugh and Jordan 2001; Deuss and Woodhouse 2004). There is some question as to whether the velocity impedance caused by the HCEn/OEn phase transition is sufficient to account for the transition (Williams and Revenaugh 2005), and this has lead to consideration of alternative mechanisms for the origin of the discontinuity (Williams and Revenaugh 2005; Ganguly and Frost 2006). However, the phase transition remains a viable candidate for some instances, at least when opx-rich harzburgites are plausible mantle lithologies (Matsukage et al. 2005), such as in continental lithosphere, subducted oceanic lithosphere, and mantle wedges. If subducted slabs and/or mantle wedges have high water contents, then the HCEn/OEn phase transition should be deflected upwards to shallower depths and our data suggest that this deflection may reduce the transition to depths of 250 km or shallower for fully saturated conditions. If such deflections are observable, they may support attribution of the X discontinuity to phase transitions in orthopyroxene.

## Conclusions

- The $H_2O$ storage capacity of HCEn at 10.2–13.4 GPa (0.13–0.67 wt. % $H_2O$) is significantly greater than those of enstatite and clinoenstatite at $P < 10$ GPa.
- At pressure ≥10 GPa, the $H_2O$ storage capacity of HCEn decreases with increasing temperature from 1,100 to 1,400°C. The inverse correlation between temperature and storage capacity is expected to be a general feature at high pressure and temperature, and is a result of dilution of the hydrous component in the coexisting fluid.
- High $a_{H2O}$ stabilises HCEn with respect to En, owing to a greater $H_2O$ storage capacity in the monoclinic (*C2/c*) phase and resulting in a depression of the phase boundary by at least 1 GPa. Displacement of the phase boundary to lower pressures may allow a test of the hypothesis that the 'X' discontinuity is caused by the OEn-HCEn phase transition in harzburgite in the mantle.

**Acknowledgments** We gratefully acknowledge the assistance of Cyril Aubaud, and Yunbin Guan during SIMS analyses at ASU and of Jinping Dong for help with the Raman spectrometer and Ellery Frahm for help with the electron microprobe. We thank Steve Jacobsen for illuminating discussions, and two anonymous reviewers for their thoughtful comments and suggestions. Parts of this work were carried out in the Minnesota Characterization Facility, which receives partial support from NSF through the NNIN program. This work supported by NSF EAR0456405.

## Appendix 1: Multi-anvil pressure calibration

The 14–8 assembly was calibrated against the Bi I–II and III–V transitions at 25°C (Piermarini and Block 1975), by reversal of the coesite-stishovite phase transformation at 1,200°C (Zhang et al. 1993) and using a high pressure fixed point defined by coexisting $(Mg,Fe)_2SiO_4$ phases at 1,400°C (Fig. 9). An additional constraint was provided by a half-bracket of the $Mg_2SiO_4$ olivine-wadsleyite phase transition at 1,200°C (Morishima et al. 1994). Following the technique described by Frost and Dolejš (2007), the high pressure fixed point was determined by analysis of coexisting phases in the $(Mg,Fe)_2SiO_4$ phase diagram. Starting materials were constructed from mixtures of dried reagent MgO, crystalline $SiO_2$, FeO and Fe metal such that each composition would form an assemblage of olivine polymorph(s), magnesiowüstite and ~10% metallic iron under the experimental conditions. Bulk Fe/(Fe + Mg) ratios were varied so as to maximise the likelihood of producing coexisting phases of $(Mg,Fe)_2SiO_4$ in the charge. The four starting compositions were loaded into a four-chambered $Al_2O_3$ capsule, as described in Frost and Dolejš (2007), and the

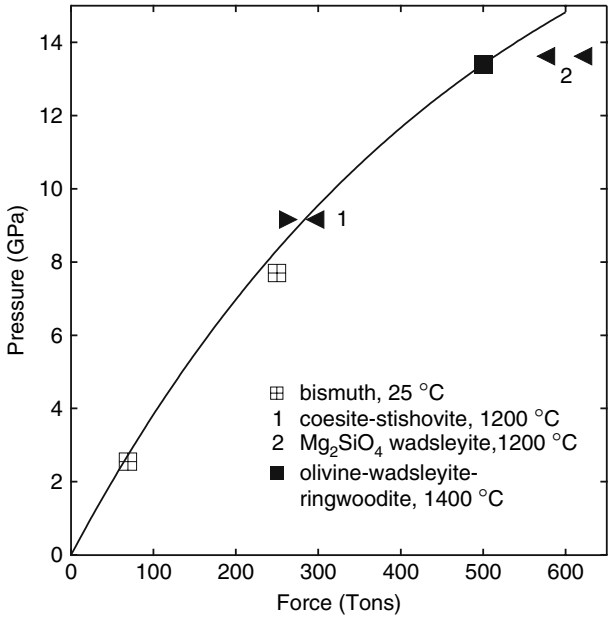


**Fig. 9** Force-pressure relationship for the 14–8 assembly. The *square symbols* represent fixed points, and each *triangle* demarcates a pressure constraint provided by phase stability

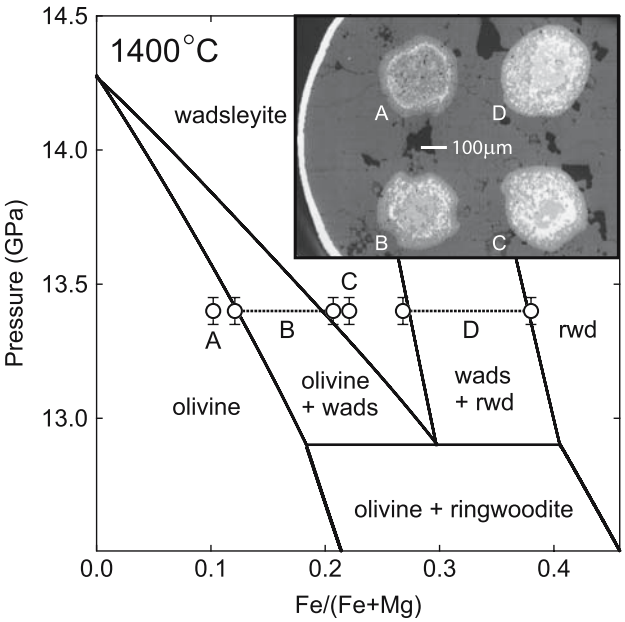


**Fig. 10** Phase diagram for $(Mg,Fe)_2SiO_4$ calculated by Frost and Dolejš (2007) using the data of Frost (2003) and Jacobs and Oonk (2001). The Fe# (Fe/(Fe + Mg)) of $(Mg,Fe)_2SiO_4$ polymorphs present in each of the four chambers of the $Al_2O_3$ capsule (labelled A-D in the inset backscattered electron image) are plotted as *circles* at a pressure that best matches the phase diagram. Coexisting mineral pairs within a chamber are connected by *dotted lines*

**Table 3** Phase compositions determined by electron microprobe

| Chamber | Phase | $n^a$ | MgO | $Al_2O_3$ | $SiO_2$ | FeO | Total | Fe# |
|---|---|---|---|---|---|---|---|---|
| A | Olivine | 11 | 49.6(4) | 0.03(1) | 40.2(4) | 10.1(4) | 99.9 | 0.102(4) |
| A | magnesiowüstite | 3 | 49.1(5) | 0.3(1) | 0.2(1) | 51.7(1) | 101.2 | 0.372(2) |
| B | Olivine | 8 | 48.4(3) | 0.03(2) | 40.0(2) | 11.9(3) | 100.3 | 0.121(3) |
| B | Wadsleyite | 7 | 41.2(2) | 0.9(3) | 38.3(2) | 19.2(1) | 99.5 | 0.207(1) |
| B | magnesiowüstite | 2 | 40.3(2) | 0.10(0) | 0.04(1) | 61.2(3) | 101.6 | 0.460(3) |
| C | Wadsleyite | 5 | 40.4(3) | 0.5(2) | 38.3(2) | 20.5(2) | 99.6 | 0.221(1) |
| C | magnesiowüstite | 3 | 32.5(4) | 0.08(2) | 0.08(9) | 67.9(4) | 100.6 | 0.540(1) |
| D | Wadsleyite | 5 | 37.6(3) | 0.66(5) | 37.6(3) | 24.5(3) | 100.3 | 0.268(3) |
| D | Ringwoodite | 19 | 30.7(3) | 0.13(1) | 36.6(5) | 33.5(5) | 101.0 | 0.380(5) |
| D | magnesiowüstite | 3 | 25.8(1) | 0.20(6) | 0.05(1) | 74.5(1) | 100.5 | 0.618(1) |

Numbers in parentheses represent 1 SD in the least significant digit of the preceding value

[a] Number of analyses

alumina capsule was wrapped in Fe foil and positioned immediately below the thermocouple junction in the 14–8 assembly. The starting materials and assembled octahedron were stored under vacuum prior to running the calibration experiment. The experiment was pressurised and heated at 1,400°C for 8 h before turning off the power supply and depressurising to ambient conditions. The capsule was recovered, sectioned with a wire saw in a plane perpendicular to the axis of the heater and prepared for electron microprobe analysis (Fig. 10, inset). The exposed areas of the capsule chambers were located within 0.3 mm of the thermocouple junction at the end of the experiment. A 20 μm rim of garnet formed at the outer edge of each chamber through reaction with the $Al_2O_3$ capsule, and metallic Fe was dispersed throughout the interior of each chamber. The compositions and Fe# for coexisting $(Mg,Fe)_2SiO_4$ polymorphs and magnesiowüstite determined by electron microprobe are given in Table 3, and the compositions of $(Mg,Fe)_2SiO_4$ polymorphs are plotted as a function of Fe# at a pressure that best matches the $(Mg,Fe)_2SiO_4$ phase diagram in Fig. 10. The uncertainty in pressure determination for this fixed point, based on the fit to the phase diagram, is estimated to be ±0.05 GPa, and the uncertainty in pressure determination using the calibration curve (Fig. 9) is estimated to be ±0.5 GPa.

## References


Angel R, Hugh-Jones D (1994) Equations of state and thermodynamic properties of enstatite pyroxenes. J Geophys Res 99:19777–19783

Angel RJ, Chopelas A, Ross NL (1992) Stability of high-density clinoenstatite at upper-mantle pressures. Nature 358:322–324

Aubaud C, Hauri EH, Hirschmann MM (2004) Hydrogen partition coefficients between nominally anhydrous minerals and basaltic melts. Geophys Res Lett 31:L20611. doi:20610.21029/22004GL021341

Aubaud C, Withers AC, Hirschmann MM, Guan Y, Leshin LA, Mackwell SJ, Bell DR (2007) Intercalibration of FTIR and SIMS for hydrogen measurements in glasses and nominally anhydrous minerals. Am Mineral 92:811–828. doi:10.2138/am.2007.2248

Bell DR, Rossman GR (1992) Water in Earth's mantle: the role of nominally anhydrous minerals. Science 255:1391–1397

Bell DR, Ihinger PD, Rossman GR (1995) Quantitative analysis of trace OH in garnet and pyroxenes. Am Mineral 80:465–474

Bell DR, Rossman GR, Maldener J, Endisch D, Rauch F (2003) Hydroxide in olivine: a quantitative determination of the absolute amount and calibration of the IR spectrum. J Geophys Res 108:2105. doi:2110.1029/2001JB000679

Bolfan-Casanova N, Keppler H, Rubie DC (2000) Water partitioning between nominally anhydrous minerals in $MgO$-$SiO_2$-$H_2O$ system up to 24 GPa: implications for the distribution of water in the Earth's mantle. Earth Planet Sci Lett 182:209–221

Bromiley GD, Bromiley FA (2006) High-pressure phase transitions and hydrogen incorporation into $MgSiO_3$ enstatite. Am Mineral 91:1094–1101

Bromiley GD, Keppler H (2004) An experimental investigation of hydroxyl solubility in jadeite and Na-rich clinopyroxenes. Contrib Mineral Petrol 147:189–200

Bromiley GD, Keppler H, McCammon C, Bromiley FA, Jacobsen SD (2004) Hydrogen solubility and speciation in natural, gem quality chromian diopside. Am Mineral 89:941–949

Chen J, Inoue T, Yurimoto H, Weidner DJ (2002) Effect of water on olivine-wadsleyite phase boundary in the $(Mg,Fe)_2SiO_4$ system. Geophys Res Lett 29:1875. doi:1810.1029/2001GL014429

Chernosky JV, Day HW, Caruso LJ (1985) Equilibria in the system $MgO$–$SiO_2$–$H_2O$—experimental determination of the stability of Mg-anthophyllite. Am Mineral 70:223–236

Dasgupta R, Hirschmann MM, Withers AC (2004) Deep global cycling of carbon constrained by the solidus of anhydrous, carbonated eclogite under upper mantle conditions. Earth Planet Sci Lett 227:73–85

Demouchy S, Deloule E, Frost DJ, Keppler H (2005) Pressure and temperature-dependence of water solubility in iron-free wadsleyite. Am Mineral 90:1084–1091

Deuss A, Woodhouse JH (2004) The nature of the Lehmann discontinuity from its seismological Clapeyron slopes. Earth Planet Sci Lett 225:295–304

Evans BW, Ghiorso MS (1995) Thermodynamics and petrology of cummingtonite. Am Mineral 80:649–663

Frost DJ (2003) The structure and sharpness of $(Mg,Fe)_2SiO_4$ phase transformations in the transition zone. Earth Planet Sci Lett 216:313–318

Frost DJ, Dolejš D (2007) Experimental determination of the effect of $H_2O$ on the 410-km seismic discontinuity. Earth Planet Sci Lett 256:182–195. doi:10.1016/j.epsl.2007.01.023

Ganguly J, Frost DJ (2006) Stability of anhydrous phase B: Experimental studies and implications for phase relations in subducting slab and the X discontinuity in the mantle. J Geophys Res 111:B06203

Hauri EH, Gaetani GA, Green TH (2006) Partitioning of water during melting of the Earth's upper mantle at $H_2O$-undersaturated conditions. Earth Planet Sci Lett 248:715–734

Hirschmann MM (2006) Water, melting, and the deep Earth $H_2O$ cycle. Annu Rev Earth Planet Sci 34:629–653

Hirschmann MM, Aubaud C, Withers AC (2005) Storage capacity of $H_2O$ in nominally anhydrous minerals in the upper mantle. Earth Planet Sci Lett 236:167–181

Hirth G, Kohlstedt DL (1996) Water in the oceanic upper mantle: implications for rheology, melt extraction and the evolution of the lithosphere. Earth Planet Sci Lett 144:93–108

Ingrin J, Latrous K, Doukhan JC, Doukhan N (1989) Water in diopside - an electron-microscopy and infrared-spectroscopy study. Eur J Mineral 1:327–341

Inoue T, H.Yurimoto, Kudoh Y (1995) Hydrous modified spinel, $Mg_{1.75}SiH_{0.5}O_4$: a new water reservoir in the mantle transition region. Geophys Res Lett 22:117–120

Irifune T, Isshiki M (1998) Iron partitioning in a pyrolite mantle and the nature of the 410-km seismic discontinuity. Nature 392:702–705

Ita J, Stixrude L (1992) Petrology, elasticity, and composition of the mantle transition zone. J Geophys Res 97:6849–6866

Jacobs MHG, Oonk HAJ (2001) The Gibbs energy formulation of the $\alpha$, $\beta$, and $\gamma$ forms of $Mg_2SiO_4$ using Grover, Getting and Kennedy's empirical relation between volume and bulk modulus. Phys Chem Miner 28:72–585

Jacobsen SD, Gilbert HJ, Ballaran TB, Frost DJ, Demouchy S, Hemley RJ (2004) The effect of water on the $P2_1/c$ to $C2/c$ high-pressure phase transition in $MgSiO_3$-clinopyroxene: implications for the mantle X-discontinuity. Eos Trans AGU 85(17):U53A-04

Jarosewich E, Nelen JA, Norberg JA (1980) Reference samples for electron microprobe analysis. Geostandards Newsl 4:43–47

Kohlstedt DL, Keppler H, Rubie DC (1996) Solubility of water in the $\alpha$, $\beta$, and $\gamma$ phases of $(Mg,Fe)_2SiO_4$. Contrib Mineral Petrol 123:345–357

Komabayashi T, Omori S (2006) Internally consistent thermodynamic data set for dense hydrous magnesium silicates up to 35 GPa, 1600 degrees C: implications for water circulation in the Earth's deep mantle. Phys Earth Planet Inter 156:89–107

Libowitzky E, Rossman GR (1996) Principles of quantitative absorbance measurements in anisotropic crystals. Phys Chem Miner 23:319–327

Libowitzky E, Rossman GR (1997) An IR absorption calibration for water in minerals. Am Mineral 82:1111–1115

Littlefield EF, Jacobsen SD, Liu Z, Hemley RJ (2005) Effects of water on the behavior of $MgSiO_3$-clinoenstatite at high pressure. Eos Trans AGU 86(52):MR41A-0899

Matsukage KN, Nishihara Y, Karato S (2005) Seismological signature of chemical differentiation of Earth's upper mantle. J Geophys Res 110:B12305. doi:12310.11029/12004JB003504

Mibe K, Fujii T, Yasuda A (2002) Composition of aqueous fluid coexisting with mantle minerals at high pressure and its bearing on the differentiation of the Earth's mantle. Geochim Cosmochim Acta 66:2273–2285

Mierdel K, Keppler H (2004) The temperature dependence of water solubility in enstatite. Contrib Mineral Petrol 148:305–311

Morishima H, Kato T, Suto M, Ohtani E, Urakawa S, Utsumi W, Shimomura O, Kikegawa T (1994) The phase boundary between $\alpha$-$Mg_2SiO_4$ and $\beta$-$Mg_2SiO_4$ determined by in situ X-ray observation. Science 265:1202–1203

Mosenfelder JL, Deligne NI, Asimow PD, Rossman GR (2006) Hydrogen incorporation in olivine from 2–12 GPa. Am Mineral 91:285–294

Paterson MS (1982) The determination of hydroxyl by infrared absorption in quartz, silicate glasses and similar materials. Bull Mineral 105:20–29

Piermarini GJ, Block S (1975) Ultrahigh pressure diamond-anvil cell and several semiconductor phase transition pressures in relation to fixed point pressure scale. Rev Sci Instrum 46:973–979

Rauch M, Keppler H (2002) Water solubility in orthopyroxene. Contrib Mineral Petrol 143:525–536

Revenaugh J, Jordan TH (2001) Mantle layering from ScS reverberations.3. The upper mantle. J Geophys Res 96:19781–19810

Shinmei T, Tomioka N, Fujino K, Kuroda K, Irifune T (1999) In situ X-ray diffraction study of enstatite up to 12 GPa and 1473 K and equations of state. Am Mineral 84:1588–1594

Skogby H, Bell DR, Rossman GR (1990) Hydroxide in pyroxene: variations in the natural environment. Am Mineral 75:764–774

Smyth JR, Frost DJ (2002) The effect of water on the 410-km discontinuity: an experimental study. Geophys Res Lett 29:1485. doi:1410.1029/2001GL014418

Smyth JR, Frost DJ, Nestola F, Holl CM, Bromiley G (2006) Olivine hydration in the deep upper mantle: Effects of temperature and silica activity. Geophys Res Lett 33:L15301. doi:15310.11029/12006GL026194

Smyth JR, Jacobsen SD (2006) Nominally anhydrous minerals and Earth's deep water cycle. In: Jacobsen SD, van der Lee S (eds) Earth's deep water cycle, Geophysical Monograph, vol 168. American Geophysical Union, pp 1–11

Stalder R (2004) Influence of Fe, Cr and Al on hydrogen incorporation in orthopyroxene. Eur J Mineralogy 16:703–711

Stalder R, Klemme S, Ludwig T, Skogby H (2005) Hydrogen incorporation in orthopyroxene: interaction of different trivalent cations. Contrib Mineral Petrol 150:473–485

Stalder R, Skogby H (2002) Hydrogen incorporation in enstatite. Eur J Mineral 14:1139–1144

Stalder R, Ulmer P, Thompson AB, Günther D (2001) High pressure fluids in the system $MgO–SiO_2–H_2O$ under upper mantle conditions. Contrib Mineral Petrol 140:607–618

Ulmer P, Stalder R (2001) The $Mg(Fe)SiO_3$ orthoenstatite-clinoenstatite transitions at high pressures and temperatures determined by Raman-spectroscopy on quenched samples. Am Mineral 86:1267–1274

Williams Q, Hemley RJ (2001) Hydrogen in the deep Earth. Annu Rev Earth Planet Sci 29:365–418

Williams Q, Revenaugh J (2005) Ancient subduction, mantle eclogite, and the 300 km seismic discontinuity. Geology 33:1–4

Woodland AB (1998) The orthorhombic to high-P monoclinic phase transition in Mg–Fe pyroxenes: Can it produce a seismic discontinuity? Geophys Res Lett 25:1241–1244

Yamada A, Inoue T, Irifune T (2004) Melting of enstatite from 13 to 18 GPa under hydrous conditions. Phys Earth Planet Inter 147:45–56

Zhang JZ, Liebermann RC, Gasparik T, Herzberg CT, Fei YW (1993) Melting and subsolidus relations of $SiO_2$ at 9–14 GPa. J Geophys Res 98:19785–19793